2D van der Waals Heterojunction of Organic and Inorganic Monolayers for High Responsivity Phototransistors

Baolin Zhao, Ziyang Gan, Manuel Johnson, Emad Najafidehaghani, Tobias Rejek, Antony George,* Rainer H. Fink, Andrey Turchanin, and Marcus Halik*

Van der Waals (vdW) heterostructures composing of organic molecules with inorganic 2D crystals open the door to fabricate various promising hybrid devices. Here, a fully ordered organic self-assembled monolayer (SAM) to construct hybrid organic–inorganic vdW heterojunction phototransistors for highly sensitive light detection is used. The heterojunctions, formed by layering MoS_2 monolayer crystals onto organic [12-(benzo[b]benzo[4,5] thieno[2,3-d]thiophen-2-yl)dodecyl)]phosphonic acid SAM, are characterized by Raman and photoluminescence spectroscopy as well as Kelvin probe force microscopy. Remarkably, this vdW heterojunction transistor exhibits a superior photoresponsivity of 475 A W^{-1} and enhanced external quantum efficiency of 1.45×10^5%, as well as an extremely low dark photocurrent in the pA range. This work demonstrates that hybridizing SAM with 2D materials can be a promising strategy for fabricating diversified optoelectronic devices with unique properties.

1. Introduction

Hybrid organic–inorganic van der Waals (vdW) heterojunctions could combine the characteristic structures and outstanding properties of both organics and inorganics, thus enable ideal

B. Zhao, T. Rejek, M. Halik
Organic Materials and Devices (OMD)
Institute of Polymer Material
Interdisziplinären Zentrums für Nanostrukturierte Filme (IZNF)
Friedrich-Alexander University of Erlangen-Nürnberg (FAU)
Cauerstr. 3, 91058 Erlangen, Germany
E-mail: marcus.halik@fau.de
Z. Gan, E. Najafidehaghani, A. George, A. Turchanin
Institute of Physical Chemistry and Abbe Center of Photonics
Friedrich Schiller University Jena
Lessingstr. 10, 07743 Jena, Germany
E-mail: antony.george@uni-jena.de
M. Johnson, R. H. Fink
Physikalische Chemie 2
Friedrich-Alexander University of Erlangen-Nürnberg (FAU)
Egerlandstr. 3, 91058 Erlangen, Germany

The ORCID identification number(s) for the author(s) of this article can be found under https://doi.org/10.1002/adfm.202105444.

interfaces and advanced functionalities useful for various applications as photodetectors,[1–4] image sensors,[5] and neuromorphic computation devices.[6] Among various building layers revealed, of notable interest is the use of 2D semiconducting transition metal dichalcogenides (TMDs) as the component owing to their unique electrical and optical performances such as high mobility and strong light–matter interactions.[7–9] Studies on TMD-based vdWs heterostructures are very much focused on the organic layer counterpart to the TMD layer, and promising performances have been demonstrated by using suitable organic layers. For instance, a remarkable photoresponsivity of 430 A W^{-1} has been revealed by coupling MoS_2 with an organic layer of zinc phthalocyanine (ZnPc).[10] Besides, a broad spectral response until the infrared region and ultrafast charge-transfer process has been observed for dye-sensitized MoS_2[11] and polymer-TMD heterostructures, respectively.[12] However, for most of the organic thin film studied, a general drawback is the poor long-range order of these organic molecules, which severely restricts the fabrication of high-performance devices.[13–15] It should be noted that this difficulty in obtaining a well-ordered organic layer for heterostructures is common for these reported preparation methods including physical vapor deposition,[1,16–20] drop-casting,[11] and soaking.[10,21] Taking the physical vapor depositing technique as an example, the source temperature, growth time, and sample location in the furnace should be accurately controlled.[19] Thus, facile and efficient methods for integrating hybrid systems with the fully ordered molecular arrangement, as well as the performances of the resulting heterostructures, are highly desirable.

Herein, by self-assembly of semiconducting organic (12-(benzo[b]benzo[4,5]thieno[2,3-d]thiophen-2-yl)dodecyl) phosphonic acid monolayer (BTBT-SAM) and then stacking with MoS_2 monolayer (1L-MoS_2) crystals, for the first time, an all 2D organic–inorganic hybrid vdW heterojunction was realized for phototransistors. The usage of a SAM as bottom layer provides clear advantages: i) the precise control of the long-range ordered organic film in single molecular thickness,[22] which effectively eliminates the charge scattering and recombination compared with multilayer organic films;[23] ii) simple processing method by the adsorption from the solution;[24] iii) the BTBT-SAM achieves effective 2D-lateral π–π interaction for charge transfer.[22] The interfacial band alignment of this
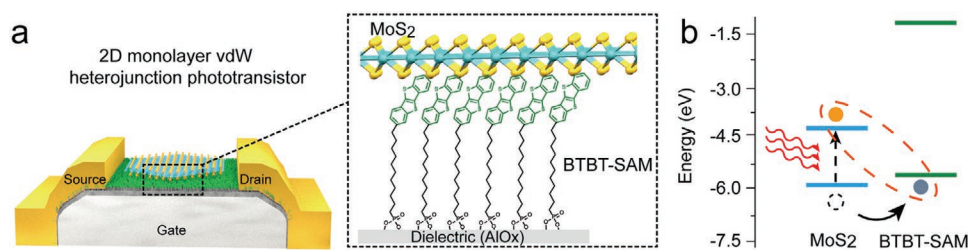
Figure 1. a) Scheme of the 1L-MoS$_2$/BTBT-SAM n–p heterojunction device. The MoS$_2$ crystal is transferred on top of the BTBT self-assembled monolayer FETs (BTBT-SAMFETs). b) The band scheme at the one-layer MoS$_2$ and BTBT-SAM interface favoring exciton dissociation upon illumination.

BTBT-SAM and the top MoS$_2$ monolayer (1L-MoS$_2$) demonstrates the formation of a type-II heterojunction. As a result, strong charge separation and transfer at the heterointerface were observed by the significantly quenched photoluminescence (PL) signals. Additionally, the surface potential quantitated by Kelvin probe force microscopy (KPFM) increases with the enhanced light intensity. The phototransistor devices show an unprecedented responsivity of 475 A W^{-1} and ultrahigh external quantum efficiency of up to 1.45×10^5% ascribed to the photogating effect. The optoelectronic properties can be easily modulated by the flexible design of the molecular structures, rendering the combination with SAM a versatile approach to investigate the light-induced interactions and physics in ultrathin semiconductor hybrid structures and facilitate the future applications of optoelectronic devices.

2. Results and Discussion

The configuration of the prepared phototransistor devices which consist of highly ordered BTBT-SAM and 1L-MoS$_2$ heterojunction is shown schematically in **Figure 1**a. To fabricate such vdW heterostructure devices, chemical vapor deposition (CVD) grown high-quality monolayer MoS$_2$ crystals [25,26] were transferred onto prefabricated BTBT-SAM field effect transistor (FET) devices. Note that the MoS$_2$ crystals are transferred in the BTBT-SAM channel region and not connected the source–drain electrodes as shown schematically in Figure 1a. The detailed fabrication process can be found in the Experimental Section. The highest occupied molecular orbital (HOMO) and the lowest unoccupied molecular orbital (LUMO) of BTBT-SAM calculated by density functional theory were −5.63 and −1.32 eV, respectively. The valence and conduction bands of 1L-MoS$_2$ (E_{VB} = −5.96 eV, and E_{CB} = −4.25 eV) are referred to literature.[27] Concerning the energy levels alignment, the prepared 1L-MoS$_2$/BTBT-SAM bilayer forms a type-II "staggered gap" heterojunction as shown in Figure 1b.
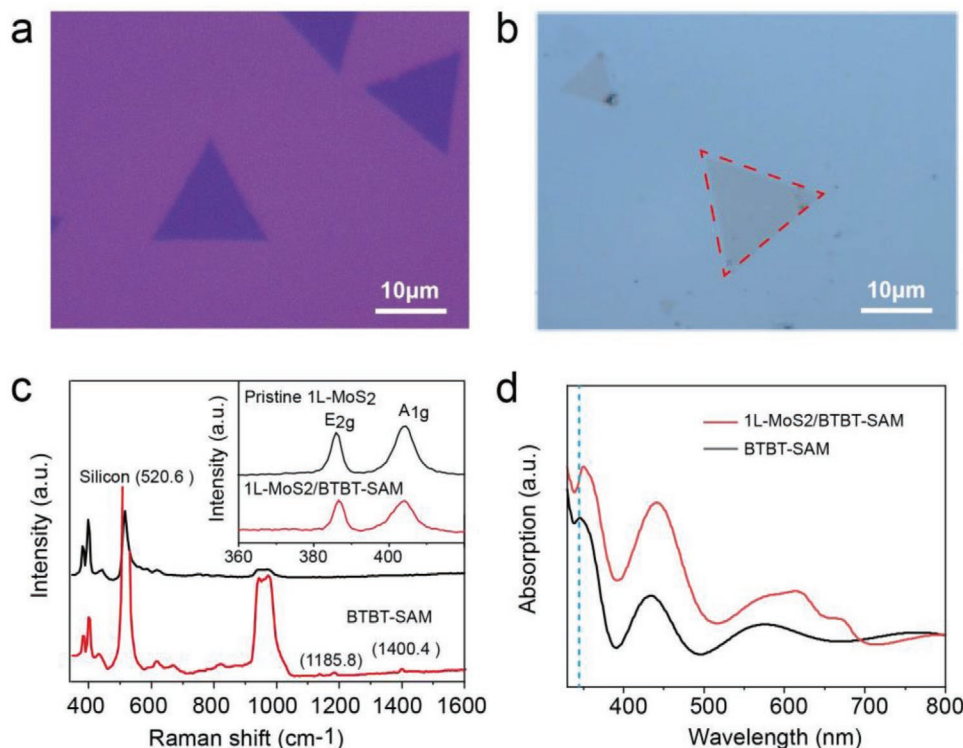
Optical images of monolayer MoS$_2$ crystals before and after transfer onto the BTBT-SAM film are shown in **Figure 2**a,b, respectively. The surface morphology and height profile were determined via atomic force microscopy (AFM) which is shown in Figure S1 (Supporting Information). The measured thickness of 0.89 nm confirms the monolayer nature of the MoS$_2$ crystals according to the previous study.[28] The successful transfer of the MoS$_2$ monolayer onto BTBT-SAM is confirmed by the height profile (Figure S1b, Supporting Information) where a consistent thickness is observed.

Raman spectroscopy was used to further confirm the formation of the monolayer stacking in the 1L-MoS$_2$/BTBT-SAM heterojunction. As shown in Figure 2c, the pristine 1L-MoS$_2$ grown on Si/SiO$_2$ by CVD shows the vibrational modes of A$_{1g}$ and E$^1_{2g}$ at 385.9 and 404.3 cm^{-1} with the interval of 18.4 cm^{-1} proving a monolayer.[29,30] After transferring the 1L-MoS$_2$ onto the BTBT-SAM, the Raman spectra shows A$_{1g}$ and E$^1_{2g}$ modes at 386.6 and 405.4 cm^{-1}, as well as the alkyl chain (−CH$_2$−CH$_2$−) at 1138 and 1185 cm^{-1}, the conjugated rings at 1400 cm^{-1} of the BTBT-SAM. Besides, the optical absorption in Figure 2d was measured by ultraviolet–visible (UV–Vis) spectroscopy. The peaks around at ≈680 nm (1.91 eV) and ≈605 nm (2.06 eV) correspond to the excitons of MoS$_2$.[2,31] Compared to the absorption of pristine BTBT-SAM, the position at around 351 nm appears slightly redshifted after 1L-MoS$_2$ transferred onto the BTBT-SAM layer. Above all, these results confirm that the single-layer MoS$_2$ was successfully transferred onto BTBT-SAM film to form monolayer 1L-MoS$_2$/BTBT-SAM heterostructures.

The interlayer interaction between the 1L-MoS$_2$ and BTBT-SAM was investigated by room temperature PL and KPFM measurements. **Figure 3**a,b shows the PL maps of the 1L-MoS$_2$ grown on Si/SiO$_2$ wafer and in the 1L-MoS$_2$/BTBT-SAM heterojunction under an excitation wavelength of 532 nm, respectively. As shown in Figure 3c, the PL spectrum shows a single sharp excitonic peak at 673 nm (1.84 eV) of monolayer MoS$_2$ crystals. Significant PL quenching occurs in the heterojunction compared to the 1L-MoS$_2$ on the silicon wafer. The as-grown single-layer MoS$_2$ crystal shows 20 times higher PL intensity than the heterojunction, suggesting the efficient exciton dissociation at the interface and charge transfer from 1L-MoS$_2$ to BTBT-SAM.[3]

In addition, the photoinduced charge separation between the 1L-MoS$_2$/BTBT-SAM heterojunction was provided by KPFM. This technique measures the local surface potential, thus the charge carrier generation and transfer inside the heterojunction can be evaluated both with and without illumination.[32,33] Figure 3d,e shows a clear difference of surface potential in the BTBT-SAM and 1L-MoS$_2$ areas. The surface potential difference (SPD) across the heterojunction is around 160 mV under dark owing to the difference in the work function of BTBT and MoS$_2$. Under illumination (λ = 406 nm), we found the measured SPD inside the 1L-MoS$_2$ crystal increases with the increased light intensity before reaching saturation at an intensity of around 0.15 mW cm^{-2}. The decrease inside the 1L-MoS$_2$ region is about 60 mV while the change of the BTBT region is negligible. This increased potential of the 1L-MoS$_2$ region confirms the optoelectrical effect taking place at the 1L-MoS$_2$/BTBT-SAM interface. Under the built-in electric field of the heterojunction, holes are expected to be transferred to the BTBT-SAM layer while electrons remain in the MoS$_2$ leading to quasi-Fermi levels shift of both materials in opposite directions.[30] As the whole substrate

ADVANCED
SCIENCE NEWS
www.advancedsciencenews.com

ADVANCED
FUNCTIONAL
MATERIALS
www.afm-journal.de

Figure 2. Optical microscopy images of CVD-grown 1L-MoS$_2$ a) on SiO$_2$/Si substrate and b) after transferring onto the BTBT-SAM substrate. The BTBT-SAM is formed on atomic-layer-deposited aluminum oxide (AlOx) on Si/SiO$_2$ wafer. c) Raman spectra of pristine 1L-MoS$_2$ (black line) and 1L-MoS$_2$/BTBT-SAM heterojunction (red line). d) UV–vis absorption recorded from BTBT-SAM (black) and 1L-MoS$_2$/BTBT-SAM heterojunction (red) fabricated on ITO glass.

is fully covered by the BTBT-SAM layer underneath the 1L-MoS$_2$ crystals, the transferred holes can be localized in the traps leading to an almost constant local surface potential outside of the 1L-MoS$_2$ crystal area. In contrast, the generated electrons transferred to the 1L-MoS$_2$ are confined inside the crystal, which leads to an enhancement in the local surface potential.[33,34]

The photoresponse properties of the 1L-MoS$_2$/BTBT-SAM vdW heterostructure phototransistor devices were investigated under ambient conditions using a homemade photocurrent measurement system. The optical microscopy image of the phototransistor is presented in **Figure 4**a, in which the 1L-MoS$_2$ is connecting only one of the electrodes or staying in between the electrodes without electrical contact. Thus, the electrical performances represented the properties of the BTBT-SAM channel when a source–drain voltage (V_d) is applied. The photocurrent is characterized by varied power intensities under a 406 nm UV light. First, the pristine BTBT-SAMFETs were fabricated and measured as a reference (Figure S2, Supporting Information). The transfer curve of the BTBT-SAMFET devices changes negligibly between dark and illumination conditions. The average mobility of BTBT-SAMFETs is 1.04×10^{-3} cm^2 V^{-1} s^{-1}. In contrast, the transfer curves of the 1L-MoS$_2$/BTBT-SAM heterojunction phototransistors exhibit a clear photoresponse behavior at the same laser intensity (Figure 4b). The threshold voltage (V_{th}) shifts toward the positive direction from −4.76 V to −4.24 V as a function of the irradiation power until saturation at about 0.155 mW cm^{-2}. The positive shift of the threshold voltage could be ascribed to the

built-in potential by photogenerated holes, which manifests a photogating mechanism in this device.[35–37]

The photosensitivity (I_p/I_{dark}), which was defined as the generated photocurrent (I_p) flowing in a transistor compared with the corresponding dark state, was detected at different light intensities ($V_d = -3$ V). As shown in Figure S3 (Supporting Information), our organic–inorganic heterojunction phototransistors show increased photocurrent with increasing light intensity. It was found that the calculated photosensitivity reaches as high as 1.07×10^3 at the illumination intensity of 0.155 mW cm^{-2}. Based on the photocurrent generation mechanisms (e.g., photovoltaic, photoconductive, and photogating effect),[38,39] the devices show a clear correlation between the photocurrent and the power density ($I_P \propto P^\alpha$, at $V_g = -7.0$ V) with $\alpha \approx 0.47$, which also confirms the existence of a strong photogating effect (Figure S4, Supporting Information).

Furthermore, the photoresponsivity (R), as one of the most important parameters of the phototransistors, was extracted by $R = \Delta I_{ph}/P_{in}$. The remarkable photoresponsivity of 475 and 232 A W^{-1} were obtained for a laser intensity of 0.05 and 0.176 mW cm^{-2} at the accumulated area ($V_g = -7$ V, $V_d = -3$ V), as presented in Figure 4d. It is notable here, to our knowledge, the photoresponsivity (475 A W^{-1}) obtained in our 1L-MoS$_2$/BTBT-SAM phototransistors is three orders of magnitude higher than that of the commercially available Si- and Ga-based UV photodetectors (0.1–0.8 A W^{-1}) and also represents as a record value among organic semiconductor–transition metal
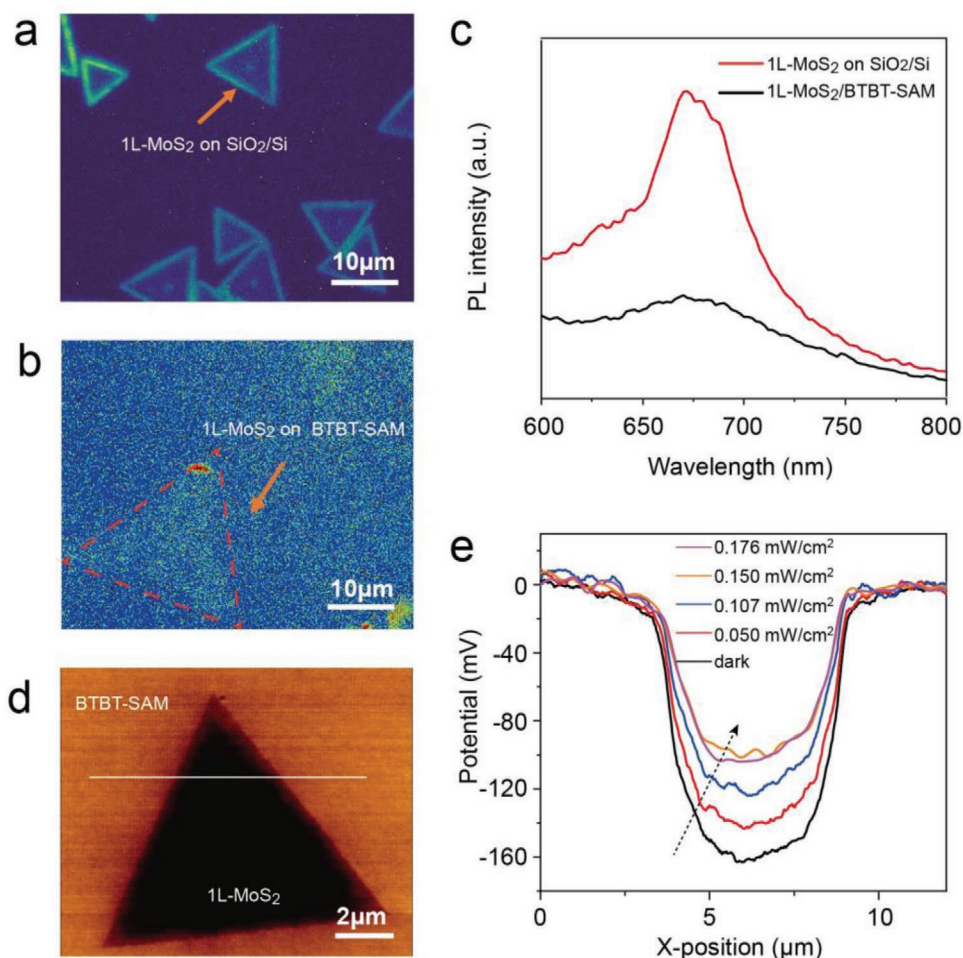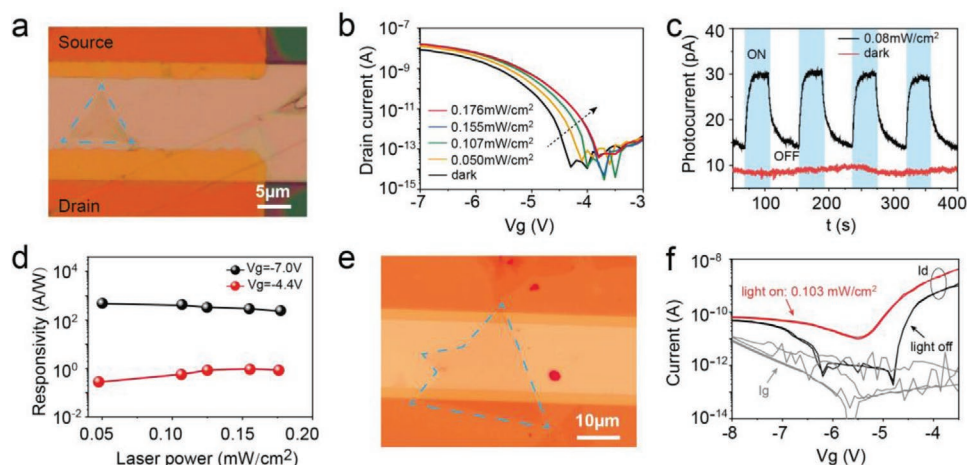
Figure 3. Photoluminescence (PL) mapping of a) CVD grown 1L-MoS$_2$ on Si/SiO$_2$ substrate and b) after subsequent transfer onto BTBT-SAM/AlOx/Si/SiO$_2$ substrate. c) Comparison of the PL spectra in the range of 600–800 nm. d) Surface potential images of 1L-MoS$_2$ after transferring onto BTBT-SAM under 0.05 mW cm^{-2} irradiation with 406 nm wavelength. e) Line scans taken across the white line in (d). The arrow indicates the SPD change with light intensities.

dichalcogenides hybrid heterojunction photodetectors (higher than 430 A W^{-1}, Table S1, Supporting Information).

The dynamic switch of drain current from dark to light was evaluated by a chopping light with different frequencies. Under illumination, the device current changes periodically from low to high accompanying the light source on and off, suggesting stable photoswitchable performances. Moreover, the devices show a clear rectifying effect and can recover to the initial state after the laser switched off (Figure 4c). The excitons are generated under illumination and separated efficiently at the hetero-interface. Subsequently, the holes are collected by BTBT-SAM, which leads to a positive shift of V_{th}. The response times for both rise and decay processes were extracted according to the time of I_{ph} increased from 10% to 90% and vice versa. From Figure S6 (Supporting Information), the response time and decay time were calculated to be 5.5 and 17.8 s, respectively. The relatively low photoresponse time of the 1L-MoS$_2$/BTBT-SAM heterostructure phototransistors may be attributed to the grain boundaries in BTBT-SAM and residual water/oxygen at the interface.[40] Moreover, the external quantum efficiency (EQE) was evaluated with the following equation

$$EQE = (I_{light} - I_{dark})hc/(qP_{in}\lambda) \tag{1}$$

in which I_{light} stands for the drain current under light condition; I_{dark} is the drain current in dark condition; h is the Planck constant; c represents the velocity of light; q is the unit charge; and λ is the excitation wavelength. The EQE (Figure S5, Supporting Information) with a value of as high as $1.45 \times 10^5\%$ shows the same tendency as the responsivity. The enhanced EQE can be explained by filling photoinduced charge carriers in trap sites inside BTBT-SAM. Overall, hybrid organic–inorganic photodetectors based on a 1L-MoS$_2$/BTBT-SAM heterojunction were successfully prepared, in which the efficient dissociation of photoinduced charge carrier and reduced recombination result in sensitive current multiplication as well as a remarkable high EQE in organic–inorganic photodetectors.[41,42] More than 20 1L-MoS$_2$/BTBT-SAM heterojunction transistor devices were characterized and they show similar device performances. Besides, the electrical performances of 1L-MoS$_2$ contacting with both source and drain electrodes were investigated for comparison (Figure 4f). The ambipolar transport behavior of 1L-MoS$_2$/BTBT-SAM heterojunction transistors with the typical

**ADVANCED
SCIENCE NEWS**

www.advancedsciencenews.com

**ADVANCED
FUNCTIONAL
MATERIALS**

www.afm-journal.de

Figure 4. Photoelectrical characterization of the 1L-MoS$_2$/BTBT-SAM phototransistors. a) Optical image of the phototransistor with 1L-MoS$_2$ only located in the channel area. b) Transfer curves of all 2D 1L-MoS$_2$/BTBT-SAM phototransistors without and with irradiation of 406 nm light. ($V_d = -3$ V, measured in ambient conditions). c) Highly reproducible photocurrent response at dark and light irradiation (incident power: 0.08 mW cm^{-2}, $V_g = -4.4$ V, $V_d = -3$ V). d) Responsivity of the hybrid 1L-MoS$_2$/BTBT-SAM phototransistor versus illumination power density at different gate biases. e) Optical image of the 1L-MoS$_2$/BTBT-SAM bilayer ambipolar phototransistor, in which the MoS$_2$ monolayer is contacting with both of the source–drain electrodes. f) Photoresponse behavior of bilayer ambipolar phototransistors.

"V" shape (measured at $V_d = -3$ V) was observed, and the devices also exhibit clear photoresponse at both regions while on/off ratio under light is lower owing to the complementary layer cannot be fully switched off.[43,44]

3. Conclusions

In summary, we presented a facile approach by composing a SAM into organic–inorganic hybrid vdW heterojunction for highly sensitive light detection. A type-II heterojunction with a highly ordered organic semiconducting monolayer underneath 1L-MoS$_2$ crystals was obtained, representing as the first all-2D hybrid vdW heterojunction phototransistors. The efficient photocarrier generation and separation were confirmed by PL and KPFM. The 1L-MoS$_2$/BTBT-SAM phototransistor exhibits an excellent photoresponsivity of 475 A W^{-1} and high external quantum efficiency at a low laser intensity, which is a record value compared to the previous reports on organic–TMDs hybrid photodetectors. Our work provides numerous design possibilities for 2D atomic-molecular layer stacking and integration through designing the structures of SAMs, rendering this novel heterostructure an exciting potential for optoelectronic devices.

4. Experimental Section

Materials: BTBT-SAM were used as received from Heraeus Precious Metals GmbH, Germany. The MoS$_2$ monolayer crystals were grown on Si/SiO$_2$ wafer by a modified CVD process in which a Knudsen-type effusion cell is used for the delivery of sulfur precursors.[26] The sulfur powder was placed in the first zone with a temperature of 250 °C and the second zone contains the MoO$_3$. The substrates were heated to the growth temperature of 750 °C and held for 15 min. The growth was carried out at atmospheric pressure under an argon flow of 100 cm^3 min^{-1}.

Heterojunction Device Preparation and Measurements: The heterojunction was prepared by transferring the MoS$_2$ monolayers on prefabricated BTBT-SAMFETs via a PMMA-assisted transfer protocol.[25,26] The fabrication process of BTBT-SAMFETs is according to the literature.[45] First, the CVD-grown monolayer on SiO$_2$/Si was spin-coated with PMMA 950K (MicroChem) at 4000 rpm, 30 s, and dried at 90 °C for 10 min twice. The PMMA/1L-MoS$_2$ film was released from the substrate by etching the SiO$_2$ in a 0.5 M KOH solution at 60 °C. After cleaning in deionized water for several times, the film was fished onto the BTBT-SAMFETs substrate, BTBT-SAM coated indium tin oxide (ITO) glass and AlOx/SiO$_2$ wafer, accordingly. Finally, the heterojunction devices were dried naturally in the fume hood overnight and heated at 60 °C for 5 min. Here, the BTBT-SAM layer was formed by immersing the oxygen-plasma-treated substrates into BTBT-phosphonic acid solution (0.05 × 10^{-3} M) for 72 h, rinsing with 2-isoproponal and blowing dry with nitrogen gas. The morphology of the BTBT-SAM can be found in a previous work.[22,46] For the SAMFETs-based optoelectronic devices, the PMMA was kept as an encapsulation layer. For other measurements, the PMMA was removed from the substrates by dissolving the PMMA in acetone, followed by rinsing with isopropyl alcohol. The UV–vis absorption spectroscopy was recorded on an Analytic Jena SPECORD 210 PLUS spectrometer at room temperature on ITO glass. Steady PL spectra and mapping were measured using a 532 nm laser diode as the excitation source. A monochromator and a microscope (100×) were used before the camera to record the photoluminescence mapping. The setup allows the recording of spectrally resolved images with a spectral resolution of 2 nm and a spatial resolution of 0.53 µm. Low-frequency Raman measurements were performed using a WITec Alpha 300R confocal microscope with a liquid-nitrogen cooled charge-coupled detector (CCD). The excitation laser wavelength was 532 nm (2 mW).

AFM and KPFM Measurements: The AFM and KPFM measurements were performed with a JPK Multimode Scanning Probe Microscopy (Nano wizard 3) in noncontact mode using Cr/Pt coated multi 75E-G tips. For KPFM measurements, a conventional amplitude modulated double pass configuration was used. In the first scan, the topography is received and in the second pass, the potential profile was measured while keeping the tip at a constant distance from the sample surface. A 406 nm laser with tunable intensity (Thorlabs Fiber-Coupled Laser Source) was used during the KPFM analysis.

Optoelectronic Characterization: The devices were measured at room temperature under ambient conditions using a homemade photocurrent measurement system. The electrical measurements were performed by

an Agilent B1500A semiconductor characterization system equipped with a manipulator probe station. The time-resolved excitation LED with a wavelength of 406 nm was connected to a wavefunction generator (South Korea, 2M-DAGATRON 7202). The light power was calibrated with a handheld power meter.

Supporting Information

Supporting Information is available from the Wiley Online Library or from the author.

Conflict of Interest

The authors declare no conflict of interest.

Data Availability Statement

Data available in article supplementary material.

[1] X. Liu, J. Gu, K. Ding, D. Fan, X. Hu, Y.-W. Tseng, Y.-H. Lee, V. Menon, S. R. Forrest, *Nano Lett.* **2017**, *17*, 3176.

[2] D. De Fazio, I. Goykhman, D. Yoon, M. Bruna, A. Eiden, S. Milana, U. Sassi, M. Barbone, D. Dumcenco, K. Marinov, A. Kis, A. C. Ferrari, *ACS Nano* **2016**, *10*, 8252.

[3] Y.-H. Lin, W. Huang, P. Pattanasattayavong, J. Lim, R. Li, N. Sakai, J. Panidi, M. J. Hong, C. Ma, N. Wei, N. Wehbe, Z. Fei, M. Heeney, J. G. Labram, T. D. Anthopoulos, H. J. Snaith, *Nat. Commun.* **2019**, *10*, 4475.

[4] K. Pei, T. Zhai, *Cell Rep. Phys. Sci.* **2020**, *1*, 100166.

[5] C. Choi, J. Leem, M. S. Kim, A. Taqieddin, C. Cho, K. W. Cho, G. J. Lee, H. Seung, H. J. Bae, Y. M. Song, T. Hyeon, N. R. Aluru, S. Nam, D.-H. Kim, *Nat. Commun.* **2020**, *11*, 5934.

[6] S. Wang, C. Chen, Z. Yu, Y. He, X. Chen, Q. Wan, Y. Shi, D. W. Zhang, H. Zhou, X. Wang, P. Zhou, *Adv. Mater.* **2019**, *31*, 1806227.

[7] J. Sun, Y. Choi, Y. J. Choi, S. Kim, J. Park, S. Lee, J. H. Cho, *Adv. Mater.* **2019**, *31*, 1803831.

[8] M. Gobbi, E. Orgiu, P. Samorì, *Adv. Mater.* **2018**, *30*, 1706103.

[9] R. Liu, F. Wang, L. Liu, X. He, J. Chen, Y. Li, T. Zhai, *Small Struct.* **2021**, *2*, 2000136.

[10] Y. Huang, F. Zhuge, J. Hou, L. Lv, P. Luo, N. Zhou, L. Gan, T. Zhai, *ACS Nano* **2018**, *12*, 4062.

[11] S. H. Yu, Y. Lee, S. K. Jang, J. Kang, J. Jeon, C. Lee, J. Y. Lee, H. Kim, E. Hwang, S. Lee, J. H. Cho, *ACS Nano* **2014**, *8*, 8285.

[12] C. Zhong, V. K. Sangwan, C. Wang, H. Bergeron, M. C. Hersam, E. A. Weiss, *J. Phys. Chem. Lett.* **2018**, *9*, 2484.

[13] J. W. Shi, H. B. Wang, D. Song, H. K. Tian, Y. H. Geng, D. H. Yan, *Adv. Funct. Mater.* **2007**, *17*, 397.

[14] H. Huang, Y. Huang, S. Wang, M. Zhu, H. Xie, L. Zhang, X. Zheng, Q. Xie, D. Niu, Y. Gao, *Crystals* **2016**, *6*, 113.

[15] A. Kumar, D. Naumenko, G. Rossi, E. Magnano, S. Nappini, F. Bondino, E. Segoloni, L. Amidani, F. d'Acapito, F. Boscherini, L. Barba, E. Pace, M. Benfatto, S. Casassa, M. Pedio, *Phys. Chem. Chem. Phys.* **2019**, *21*, 22966.

[16] T. Zhu, L. Yuan, Y. Zhao, M. Zhou, Y. Wan, J. Mei, L. Huang, *Sci. Adv.* **2018**, *4*, eaao3104.

[17] D. Jariwala, S. L. Howell, K.-S. Chen, J. Kang, V. K. Sangwan, S. A. Filippone, R. Turrisi, T. J. Marks, L. J. Lauhon, M. C. Hersam, *Nano Lett.* **2016**, *16*, 497.

[18] F. Liu, W. L. Chow, X. He, P. Hu, S. Zheng, X. Wang, J. Zhou, Q. Fu, W. Fu, P. Yu, Q. Zeng, H. J. Fan, B. K. Tay, C. Kloc, Z. Liu, *Adv. Funct. Mater.* **2015**, *25*, 5865.

[19] D. He, Y. Pan, H. Nan, S. Gu, Z. Yang, B. Wu, X. Luo, B. Xu, Y. Zhang, Y. Li, Z. Ni, B. Wang, J. Zhu, Y. Chai, Y. Shi, X. Wang, *Appl. Phys. Lett.* **2015**, *107*, 183103.

[20] J. Pak, J. Jang, K. Cho, T.-Y. Kim, J.-K. Kim, Y. Song, W.-K. Hong, M. Min, H. Lee, T. Lee, *Nanoscale* **2015**, *7*, 18780.

[21] J. Choi, H. Zhang, J. H. Choi, *ACS Nano* **2016**, *10*, 1671.

[22] T. Schmaltz, A. Y. Amin, A. Khassanov, T. Meyer-Friedrichsen, H.-G. Steinrück, A. Magerl, J. J. Segura, K. Voitchovsky, F. Stellacci, M. Halik, *Adv. Mater.* **2013**, *25*, 4511.

[23] D. Rhodes, S. H. Chae, R. Ribeiro-Palau, J. Hone, *Nat. Mater.* **2019**, *18*, 541.

[24] S. Najmaei, X. Zou, D. Er, J. Li, Z. Jin, W. Gao, Q. Zhang, S. Park, L. Ge, S. Lei, J. Kono, V. B. Shenoy, B. I. Yakobson, A. George, P. M. Ajayan, J. Lou, *Nano Lett.* **2014**, *14*, 1354.

[25] S. Shree, A. George, T. Lehnert, C. Neumann, M. Benelajla, C. Robert, X. Marie, K. Watanabe, T. Taniguchi, U. Kaiser, B. Urbaszek, A. Turchanin, *2D Mater.* **2019**, *7*, 015011.

[26] A. George, C. Neumann, D. Kaiser, R. Mupparapu, T. Lehnert, U. Hübner, Z. Tang, A. Winter, U. Kaiser, I. Staude, A. Turchanin, *J. Phys. Mater.* **2019**, *2*, 016001.

[27] Y. Liu, P. Stradins, S.-H. Wei, *Sci. Adv.* **2016**, *2*, e1600069.

[28] A. George, M. V. Fistul, M. Gruenewald, D. Kaiser, T. Lehnert, R. Mupparapu, C. Neumann, U. Hübner, M. Schaal, N. Masurkar, L. M. R. Arava, I. Staude, U. Kaiser, T. Fritz, A. Turchanin, *NPJ 2D Mater. Appl.* **2021**, *5*, 15.

[29] H. Li, J. Wu, X. Huang, Z. Yin, J. Liu, H. Zhang, *ACS Nano* **2014**, *8*, 6563.

[30] K. Zhang, T. Zhang, G. Cheng, T. Li, S. Wang, W. Wei, X. Zhou, W. Yu, Y. Sun, P. Wang, D. Zhang, C. Zeng, X. Wang, W. Hu, H. J. Fan, G. Shen, X. Chen, X. Duan, K. Chang, N. Dai, *ACS Nano* **2016**, *10*, 3852.

[31] D. Y. Qiu, F. H. da Jornada, S. G. Louie, *Phys. Rev. Lett.* **2013**, *111*, 216805.

[32] K. Maturová, M. Kemerink, M. M. Wienk, D. S. H. Charrier, R. A. J. Janssen, *Adv. Funct. Mater.* **2009**, *19*, 1379.

[33] K. Chen, X. Wan, J. Wen, W. Xie, Z. Kang, X. Zeng, H. Chen, J.-B. Xu, *ACS Nano* **2015**, *9*, 9868.

[34] E. J. Spadafora, R. Demadrille, B. Ratier, B. Grévin, *Nano Lett.* **2010**, *10*, 3337.

[35] C. Wang, X. Ren, C. Xu, B. Fu, R. Wang, X. Zhang, R. Li, H. Li, H. Dong, Y. Zhen, S. Lei, L. Jiang, W. Hu, *Adv. Mater.* **2018**, *30*, 1706260.

[36] V. Podzorov, V. M. Pudalov, M. E. Gershenson, *Appl. Phys. Lett.* **2004**, *85*, 6039.

[37] B. Yang, Y. Lu, D. Jiang, Z. Li, Y. Zeng, S. Zhang, Y. Ye, Z. Liu, Q. Ou, Y. Wang, S. Dai, Y. Yi, J. Huang, *Adv. Mater.* **2020**, *32*, 2001227.

[38] C. Xie, C.-K. Liu, H.-L. Loi, F. Yan, *Adv. Funct. Mater.* **2020**, *30*, 1903907.

[39] P. Yu, Q. Zeng, C. Zhu, L. Zhou, W. Zhao, J. Tong, Z. Liu, G. Yang, *Adv. Mater.* **2021**, *33*, 2005607.

[40] J. Jiang, N. Li, J. Zou, X. Zhou, G. Eda, Q. Zhang, H. Zhang, L.-J. Li, T. Zhai, A. T. S. Wee, *Chem. Soc. Rev.* **2019**, *48*, 4639.

[41] M. Yang, J. Wang, Y. Zhao, L. He, C. Ji, X. Liu, H. Zhou, Z. Wu, X. Wang, Y. Jiang, *ACS Nano* **2019**, *13*, 755.

[42] M. A. Iqbal, A. Liaqat, S. Hussain, X. Wang, M. Tahir, Z. Urooj, L. Xie, *Adv. Mater.* **2020**, *32*, 2002628.

[43] J. Zaumseil, H. Sirringhaus, *Chem. Rev.* **2007**, *107*, 1296.

[44] S. Z. Bisri, C. Piliego, J. Gao, M. A. Loi, *Adv. Mater.* **2014**, *26*, 1176.

[45] T. Schmaltz, B. Gothe, A. Krause, S. Leitherer, H. G. Steinrück, M. Thoss, T. Clark, M. Halik, *ACS Nano* **2017**, *11*, 8747.

[46] B. Zhao, B. Gothe, M. Sarcletti, Y. Zhao, T. Rejek, X. Liu, H. Park, P. Strohriegl, M. Halik, *Adv. Electron. Mater.* **2020**, *6*, 2000515.